Detection of flow separation and stagnation points using artificial hair sensors

D M Phillips[1,2]**, C W Ray**[3]**, B J Hagen**[4,5]**, W Su**[6]**, J W Baur**[1] **and G W Reich**[4]

[1] Air Force Research Laboratory, Materials and Manufacturing Directorate, Wright-Patterson AFB, OH 45433, USA
[2] University of Dayton Research Institute, 300 College Park, Dayton, OH 45469, USA
[3] Jelec, Inc. 16901 Park Row, Houston, TX 77084, USA
[4] Air Force Research Laboratory, Aerospace Systems Directorate, Wright-Patterson AFB, OH 45433, USA
[5] Sierra Lobo, Wright Executive Center, 3000 Presidential Drive, Suite 390, Fairborn, OH 45324, USA
[6] University of Alabama, Department of Aerospace Engineering and Mechanics, Tuscaloosa, AL 35487, USA

E-mail: gregory.reich.1@us.af.mil

CrossMark

Abstract

Recent interest in fly-by-feel approaches for aircraft control has motivated the development of novel sensors for use in aerial systems. Artificial hair sensors (AHSs) are one type of device that promise to fill a unique niche in the sensory suite for aerial systems. In this work, we investigate the capability of an AHS based on structural glass fibers to directly identify flow stagnation and separation points on a cylindrical domain in a steady flow. The glass fibers are functionalized with a radially aligned carbon nanotube (CNT) forest and elicit a piezoresistive response as the CNT forest impinges on electrodes in a micropore when the hair is deflected due to viscous drag forces. Particle image velocimetry is used to measure the flow field allowing for the resulting moment and force acting on the hair to be correlated with the electrical response. It is demonstrated that the AHS provides estimates for the locations of both the stagnation and separation in steady flow. From this, a simulation of a heading estimation is presented to demonstrate a potential application for hair sensors. These results motivate the construction of large arrays of hair sensors for imaging and resolving flow structures in real time.

Keywords: hair sensor, carbon nanotube array, piezoresistive transduction, stagnation point, separation point, heading estimation

(Some figures may appear in colour only in the online journal)

1. Introduction

Recently developed artificial-hair flow sensors promise to provide a superior means of measuring aerodynamic flow fields directly, including important flow features such as stagnation and separation points and regions. Artificial hair sensors (AHSs) have been extensively studied (Dickinson 2010, Dickinson *et al* 2012a, 2012b, Qualtieri *et al* 2012, Rizzi *et al* 2013, DeVries *et al* 2014, Maschmann *et al* 2014, Devaraj *et al* 2015, Droogendijk *et al* 2015 are all recent examples but by no means an exhaustive list) for both air and underwater applications. In particular, the work of Dagamseh *et al* (2012) is interesting for using AHSs for

aerodynamic state estimation. In this work, we offer a preliminary investigation of using AHSs based on structural glass fibers coated with a radially aligned forest of carbon nanotubes (CNTs) to identify the location of stagnation and separation on a quasi-2D domain through piezoresistive transduction. Specifically, we generate a steady flow past a cylinder and measure both the sensor electrical response with a source meter and the flow field stimulating the hair using particle image velocimetry (PIV). The results are correlated to investigate the potential of using AHSs for flow feature identification.

Engineered flight systems currently utilize sensors for situational awareness and state/parameter estimation, but the

number of sensors is limited and the sensors are comparatively expensive. Emphasis is currently placed on point-wise sensor accuracy rather than redundancy. Hot film/wire anemometers are examples of accurate, point-wise technologies that are already used extensively in industry for aerodynamic control and estimation. In contrast to engineered systems, biology generally employs redundancy in both control and estimation systems (Bekey 2005). For many of the same reasons biology depends upon redundancy, there are several reasons to consider redundant, distributed sensory systems for flight control. First and foremost, redundancy provides robustness to sensor failure, which is a systemic problem in systems with very few, high-grade sensors. Redundancy also provides more information regarding estimated quantities; redundant sensory arrays offer the potential to provide superior temporal and spatial estimates of quantities and phenomena, even with individual sensors of inferior accuracy.

Such data are becoming increasingly important with the development of low inertia vehicles, such as small unmanned aerial vehicles. These vehicles are intended to operate in complex terrain, such as city streets and forests, and are particularly susceptible to wind gusts and other flow disturbances. Contemporary sensors are adequate for waypoint navigation, but do not have the fidelity for the control feedback to match natural fliers, such as birds, insects, and bats. D'Angelo *et al* have demonstrated the reliance of bats on feedback from hair sensors (Sterbing-D'Angelo 2011). AHSs require hairs that can establish a strong aero-elastic connection to the boundary layer surrounding the vehicle and a transduction mechanism that is both fast and sensitive enough to transduce information about the aerodynamic state for enhanced flight control.

The material and physical properties of structural fibers makes them attractive for use in AHS applications. The high specific modulus of carbon and glass fibers coupled with a diameter of less than 10 μm allows for them to react quickly to changes in the boundary layer. Dickinson *et al* (2012b) predict that a 2.2 mm long T650 fiber in a Stokes oscillatory layer in air will remain in phase with the fluid up to 1 kHz. The current work builds upon the predictions and focuses on the electro-mechanical response of the CNT forest to a flow as the hair is moved through a space rich in flow features. To address this, we investigate the capability of AHSs to identify flow features on a cylindrical domain in a flow. It will be demonstrated practically that such sensors offer the capability of wide flow field imaging and identification of critical flow structures and phenomena. Such capabilities provide options to improve current flight estimation and control systems or even open the door for new flight control strategies in which widely distributed, cheap, noisy, perhaps best described as 'insect-grade' sensors are used to realize a robust fly-by-feel paradigm.

2. Background

Modern aircraft control systems rely upon inertial sensors and onboard algorithms for estimating relative body state,

including position and velocity, and phenomenological models for ascertaining local flow regime characteristics. Direct measurement of flow in real-time at more than a few locations has been burdensome until recently; the advent of miniaturized hot-film anemometers and now AHSs has made it possible. Such sensors might be placed over the surface of a flying body and be used to measure local flow at almost any point, without disturbing or compromising efficiency and/or stability. Large arrays of such sensors can provide direct measurement of flow features, effectively imaging the local flow field from which specific patterns provide critical information about the flow and current relative body state.

The benefits of identifying critical flow features are beginning to be realized as sensors are developed with the capability of non-invasive, wide-field measurements. In a steady flow, the geometry of a body determines the local flow field, where any aerodynamic disturbance to the body must modify the local flow field. Therefore if the local flow field is measured directly, it may provide critical information not only about relative body state, but may provide the means of sensing disturbances as they propagate throughout an array of sensors and rejecting them via a control system. The stagnation and separation points on a body provide a feature-rich space to study as their location is entirely dependent on body and flow-field state.

Control schemes utilizing this concept were initiated theoretically by Goman and Khrabrov (1994) and experimentally pursued by Mangalam (2003), Mangalam *et al* (2008), the latter of which utilized hot film anemometers to measure a large area of a wing in flight and offered direct observation of the stagnation and separation regions. These locations were then used in phenomenological models with empirically determined coefficients to predict aerodynamic coefficients as functions of flow feature locations, such as those sketched in figure 1.

2.1. Imaging a flow field

The ability to image an entire flow field over a surface has applications inside and out of the laboratory. Separation regions could be quickly identified along with other flow features that strongly influence flight. With direct measurement, such identification would no longer rely upon any phenomenological models to infer the total flow field. Attempts to determine and control separation regions are abundant in the literature and the ability to accurately determine specific regions for control provides an opportunity for optimization and energy savings. By observing an entire flow field directly, the problem of estimating relevant aerodynamic information may reduce to image recognition.

It should be noted that there are striking similarities between the flow field image concept described above and that of optic flow, which is the current theory of insect visual navigation. Many insects, including flies, navigate using what is best described as a matched filter system, tuned to specific motions in the insect visual field. Compound eyes provide many simultaneous measurements of the dynamic visual (spatial) field from which simplified vector fields are
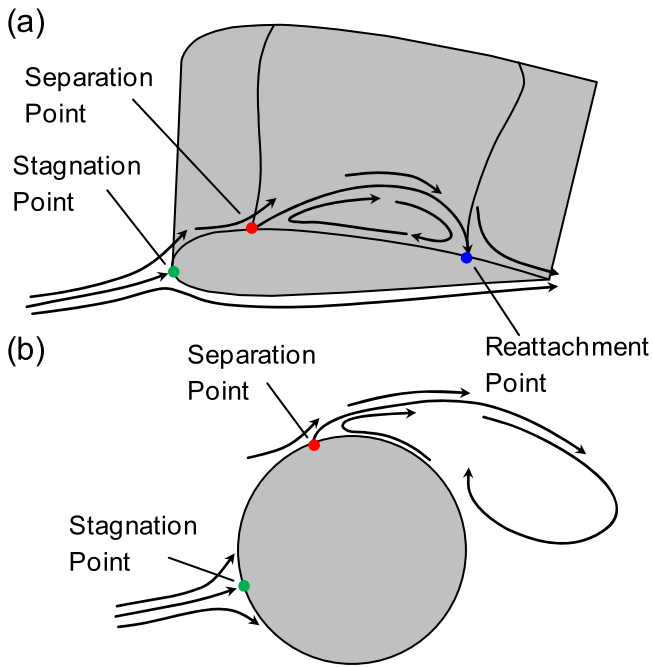
(a)

(b)

Figure 1. Stagnation, separation, and in the case of an airfoil (a), reattachment points. A cylinder (b) generates the same flow phenomena in a comparatively stable manner for study.

computed to provide relative environmental and kinematic information (Conroy *et al* 2009). In a similar manner, AHSs may provide relative flow information from which relevant parameters can be identified.

2.2. Measurement using artificial hair

It is now well-known that biological models utilize microscopic hairs for wind orientation and turbulence detection, among other adaptations. Sterbing-D'Angelo *et al* (2011) investigated the use of hairs by bats for turbulence detection and studied the consequences of hair removal on bat flight. The flight metrics for the bats were substantially degraded after hair removal, indicating the reliance of the animal on the feedback that the hairs provide. Other animals utilizing hair or hair-like structures for sensing flows include both insects and fish (Pitcher *et al* 1976, Casas *et al* 2010, Tao and Yu 2012).

　　The last decade has seen an explosion of work related to AHSs. Excellent reviews are provided by Tao and Yu (2012) and especially Rizzi *et al* (2015) with interesting experimental and theoretical analyses provided by Casas *et al* (2010) and Dickinson (2010). Some groups have devised several designs for single hairs and arrays of hairs for flow-sensors, some of which have been implemented successfully in flow experiments (Krijnen *et al* 2013, Tao and Yu 2012). However until recently, most of the research has been limited to material and mechanical design studies. Several groups have now begun investigating the identification of aerodynamic phenomena and aerodynamic control/estimation strategies that utilize AHSs (Keshavan and Humbert 2010, Dickinson *et al* 2012a, DeVries *et al* 2014). Computational analysis has yielded
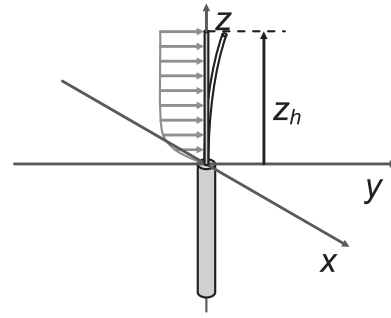

Figure 2. Artificial hair sensor undergoing deflection due to incident fluid flow.

promising results indicating that such sensors can be used for boundary layer and flow state estimation.

2.3. Artificial hair design

Continuing with the bio-inspired concept, our group has designed and constructed AHSs from micron-scale glass fibers coated with a radially aligned CNT forest. Ehlert *et al* (2011) and Maschmann *et al* (2012) previously demonstrated a piezoresistive response from planar arrays of vertically aligned CNTs and hair sensors similar to the ones used in this work. For our sensor, electrodes in an accompanying micropore allow for a piezoresistive response of the CNTs as the hair is deflected. Figure 2 depicts a hair sensor undergoing deflection due to drag forces. As the hairs are effectively cantilevered from a surface, they protrude into and potentially through a boundary layer (depending on hair length and boundary layer thickness), as illustrated alongside the hair. Thus, fluid motion induces drag upon the hair, causing a moment and shear force to exist at the hair base.

　　With the coordinate system and origin in figure 2, the total exposed hair length is z_h and drag upon the hair per unit length (drag normal to the hair axis as a function of z) is represented by $\delta(z)$. The drag upon the hair can be integrated along the exposed length to yield

$$M_x = \int_0^{z_h} \delta(z) z \, \mathrm{d}z , \tag{1}$$

$$F_y = \int_0^{z_h} \delta(z) \, \mathrm{d}z , \tag{2}$$

where M_x and F_y are the moment about the *x*-axis and force along the *y*-axis, respectively. The drag is a function of Reynolds number and is classically defined as

$$\delta(z) = \frac{1}{2}\rho(v_{\mathrm{tan}})^2 C_D d_{\mathrm{h}}, \tag{3a}$$

$$C_D = \left(\frac{\nu}{d_{\mathrm{h}}}\right)^{\frac{2}{3}} e^{\frac{5}{2}} (v_{\mathrm{tan}})^{-\frac{2}{3}}, \tag{3b}$$

where ρ is fluid density, v_{tan} is the magnitude of the flow velocity vector normal to the hair center axis (scalar) at height z, C_D is the coefficient of drag that is empirically determined and combines both form and skin drag, d_{h} is the diameter of the hair, and ν is the kinematic viscosity of air. Dickinson *et al* (2012a) demonstrated that equation (3b) provided a good
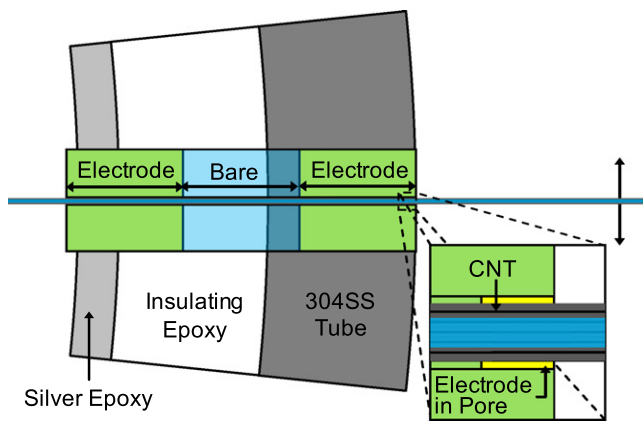
Figure 3. A cutaway diagram depicting a glass capillary with electrodes inserted into a 304SS cylinder. The outside electrode is the cylinder wall and the inside electrode consists of silver epoxy. The electrodes inside of the pore are depicted in the inset.

estimation of C_D for Reynolds numbers ranging from 0.1 to 10. By measuring the moment, force, or some combination of the two, the flow velocity profile at the hair location can be inferred. Therefore, as the nanotube forest is deformed due to aerodynamic loading of the exposed hair structure, the piezoresistance can be measured and the results can be correlated to the flow measured with PIV.

3. Experimental setup

A cylinder with an AHS mounted normal to the surface was chosen in this work to provide both stagnation and separation flow features as indicated in figure 1. The inherent symmetry of the cylinder allows for a single AHS to sample all of the flow features by simply rotating about the cylinder axis. The actual cylinder used for this work was drawn 304 stainless steel tubing with a smooth finish and a 12.7 mm (0.5 in.) outer diameter (D_c). The cylinder was designed as three pieces that fit together seamlessly. The middle section housed the AHS and had a 0.508 mm (0.020 in.) wall thickness and a 19.1 mm (0.75 in.) length. The bottom and top section had a 1.24 mm (0.049 in.) wall thickness and lengths of 142.9 mm (5.625 in.) and 130.2 mm (5.125 in.), respectively. The cylinder was mounted vertically from the floor of the wind tunnel and the AHS was 152.4 mm (6 in.) from the bottom. All of the wires for the AHS were inside of the cylinder and exited the wind tunnel through the floor.

The AHS section of the cylinder was constructed as in figure 3. A fused silica microcapillary (Polymicro Technologies, Phoenix, AZ, USA) with a 25 μm ID, a 360 μm OD, and a 1.4 mm length housed the electrodes for the AHS. The electrodes were formed by sputter coating Au–Pd onto both ends of the micro capillary with the center masked to leave that part of the capillary bare. The ends of the microcapillary were held at 45° to the sputter target and each end was sputter coated four times while rotating the microcapillary about its center axis to promote even coverage both on the outside and
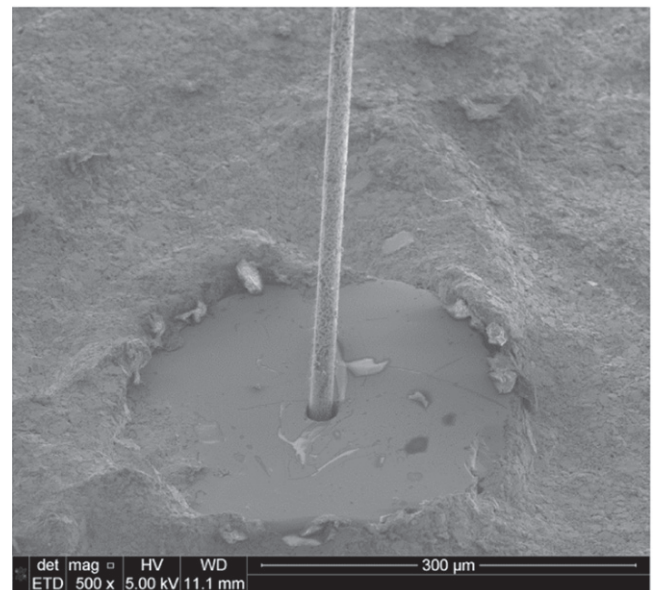

Figure 4. SEM image of the CNT coated fiber protruding from the microcapillary mounted in the 12.7 mm OD cylinder.

inside of the pore. The pore was coated to a depth of approximately 25 μm as determined by the line of sight.

The AHS section of the cylinder was drilled with a #80 bit (0.0135 in.) and the outer electrode was electrically and physically bonded to the stainless steel cylinder with H20E silver epoxy (Epoxy Technology, Inc., Billerica, MA, USA). The rear of the microcapillary was first surrounded by a layer of electrically insulating epoxy followed by a final layer of H20E silver epoxy to connect to the inner electrode as in figure 3. Two wires were bonded to the inner electrode and two were bonded to the stainless steel cylinder. The inner and outer electrodes were electrically isolated at this point since the conductive hair had not yet been installed.

The structural glass fibers for this work were obtained from a spool of 933-AA-750 glass fiber (agy, Aiken, SC, USA) and had an OD of 9 μm. Ehlert *et al* (2013) and Maschmann *et al* (2014) have described the CNT growth process for the fibers. These particular fibers were coated with 200 cycles of alumina via an atomic layer deposition process before the CNT growth in a tube furnace. For this particular batch, the tube furnace was injected with 0.690 ml of 5% (w/w) ferrocene in xylene at 2.5 ml hr^{-1}. A fiber from the resulting batch was selected and threaded into the pore of the microcapillary, leaving a length of 1 mm protruding. The conductivity and response to air currents were verified. An SEM image of the actual AHS is shown in figure 4. The outer diameter of the CNT coated fiber (d_h) was 17.6 μm.

The cylinder assembly containing the mounted AHS was firmly fixed in an Aerolab Educational Wind Tunnel (Aerolab LLC, Laurel, MD, USA) test section that has a cross-section of 11.5 in × 11.5 in and is 24 in long. The two side walls each contain large windows in addition to a small window in the ceiling. One of the side windows (not needed for PIV) was blanked out to reduce laser reflection and ambient light. The electrical leads for the AHS were contained within the sealed
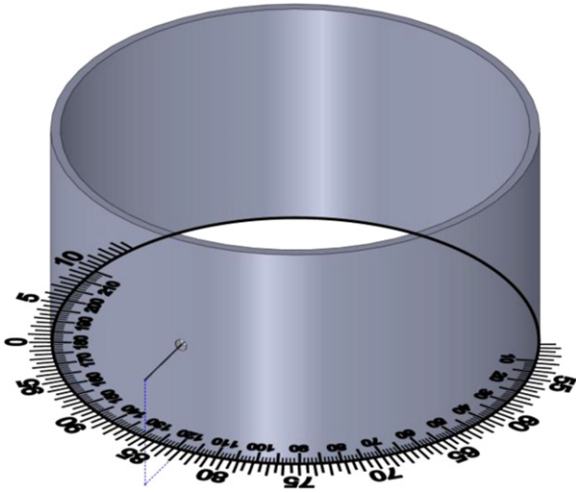
Figure 5. Diagram of an AHS on a cylinder (hair length greatly exaggerated) with respect to the alignment protractor.
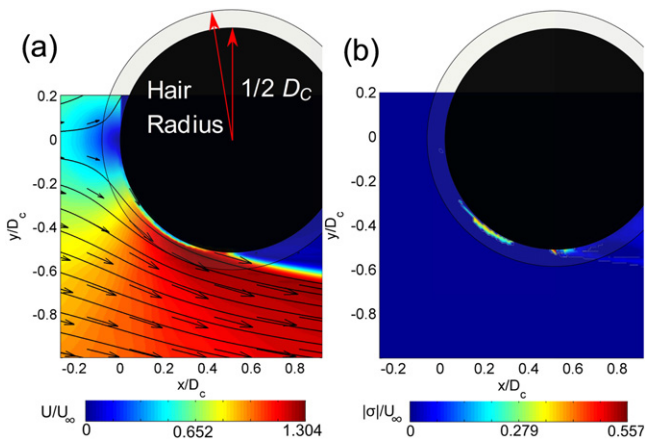

Figure 6. Streamlines and vectors from the PIV data (a) indicate flow direction and path around a cylinder with the hair radius indicated. The standard deviation of the norm of the flow velocity (b) from the PIV is small in comparison.

Figure 7. Mean AHS response (pie chart inset) versus the flow field around the cylinder.

cylinder body. The cylinder was floor mounted, but spanned the entire test section (floor to ceiling) to best ensure flow symmetry and place the AHS in the center of the test section. The cylinder was located at the center of wind tunnel test section and a protractor on the test section floor was used to carefully set the azimuthal position of the AHS on the cylinder. An illustration of the alignment setup is provided in figure 5, where position 0 points upstream of the flow. Note that the index on the protractor is not degree measurements but instead divides the cylinder circumference into 100 intervals, each corresponding to $3.6°$. This was sufficient resolution for the manual adjustment limits with the current setup.

During the experiments, the wind tunnel velocity was controlled about a set point of 15 mph. The electrical current flowing through the AHS was measured with a Keithley 2410 source meter (Keithley Instruments, Inc., Cleveland, OH, USA) at a rate of 10 Hz with 0.5 VDC stimulation. The 4-wire
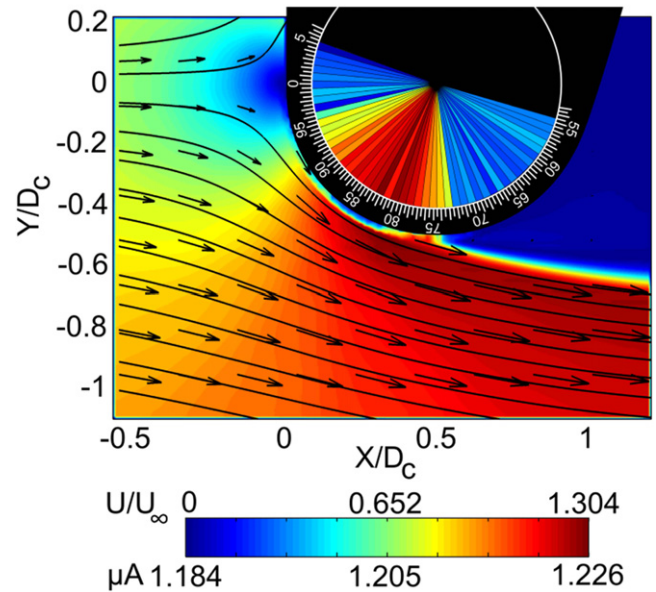
mode was used to minimize any effects of the leads on the measurements. The 51 angles corresponding to protractor locations 55 through 5, as indicated in figure 5, were randomized for order. Each of the angles was manually set and electrical data were collected for 30 s after the flow stabilized. After the experimental grid was completed, the entire experiment was repeated with a new randomized order of angular positions for a total of five runs. Randomization provided a means of ascertaining drift. The entire data collection process for the five sets spanned 6 hr and demonstrated only slight drift during that period.

Two component PIV measurements were acquired in a horizontal, stream-wise plane near the hair sensor (wind tunnel center-line). The laser used in this experiment was an Nd:YAG operating at 532 nm (New Wave Solo 120 mJ/ pulse, ESI, Portland, OR, USA). The short focal distance allowed for a very thin sheet ($<$1 mm), reducing out of plane measurement error. The laser sheet was projected from one side of the wind tunnel and precisely aligned to a plane normal to the cylinder axis. The camera was a PCO.1600 (1600×1200 pixel CCD, PCO-TECH, Inc., Romulus, MI, USA) with a 105 mm lens ($f/4.0$). It was mounted above the test section and aligned perpendicularly to the laser sheet. The field of view was about $23\,\text{mm} \times 17\,\text{mm}$. The flow was seeded with a Corona ViCount 5000 (Corona Integrated Technologies Inc., West Vancouver, B.C. Canada), that produces particles of roughly 0.2–0.5 μm in diameter from a mineral oil based fluid. A sequence of 2000 image pairs was acquired at 10 Hz, with an inter-frame delay of 20 μs. The data was processed using LaVision's DaVis 8, with 32×32 pixel interrogation regions (0.46 mm spatial resolution) and a 75% overlap to oversample the images.
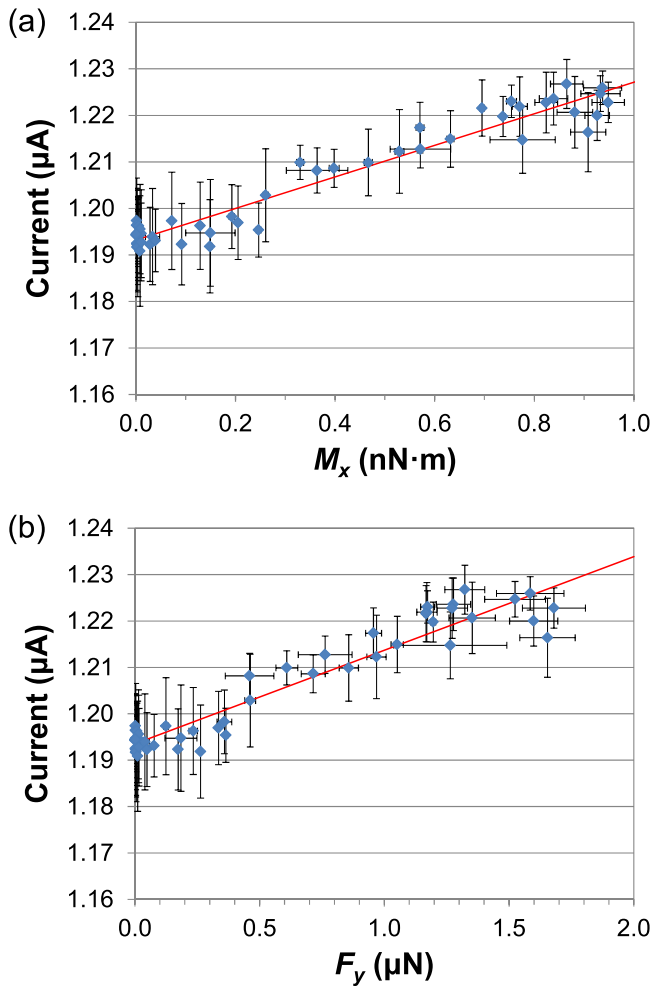
Figure 8. The AHS response with one sigma bars versus the average (a) moment and (b) force acting on the hair.

Figure 9. The (a) total force and moment acting on the hair and (b) the electrical response as a function of heading angle.

4. Results and discussion

The flow velocity mean and variance were computed from the PIV data sets as in figure 6. The variance in the velocity field was small compared to the magnitude of the velocity with the exception of the region immediately surrounding the cylinder. The main contributors to this error are laser reflection from the cylinder and the domain size used for the PIV calculations. The Reynolds number around the cylinder was about 5000–6000, which yielded a stable position for the boundary layer separation without vortex shedding. The maximum Reynolds number for the hair was about 16.7.

The average velocity field was used to approximate the moment and force acting on the hair at each of the 51 experimental positions. This was accomplished by computing the velocity magnitude normal to the hair axis using a cross product. This normal component was used with equation (3) to calculate the drag as a function of position along the hair axis. These values were then numerically integrated to calculate the total moment and force at the hair base per equations (1) and (2), respectively.
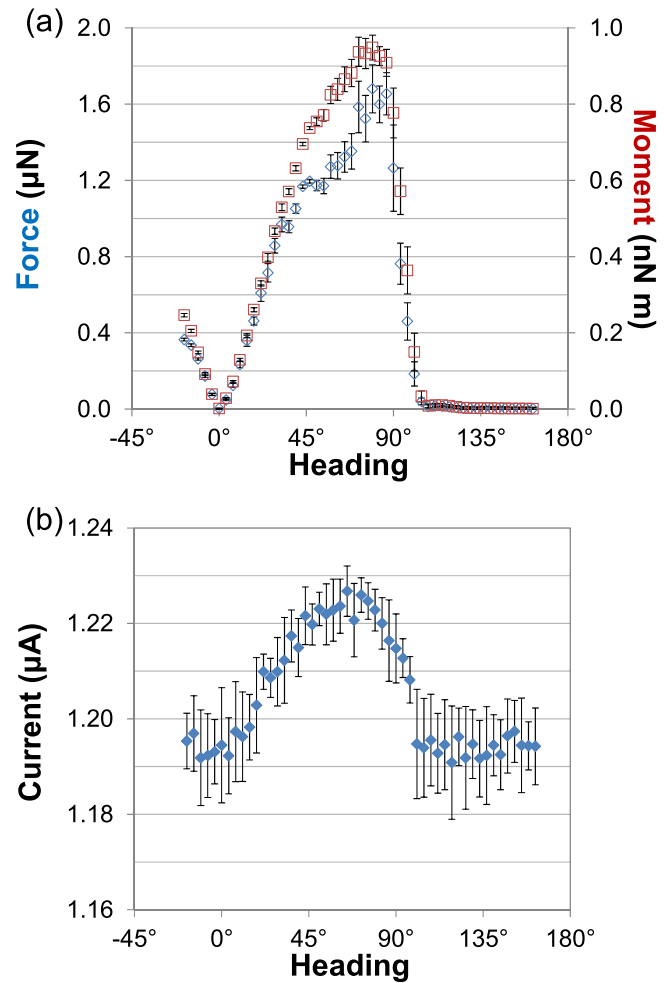
For the numerical integration, the trapezoidal integration method was used to approximate relevant integrals. A grid corresponding to 1/100 total hair length or approximately 0.01 mm was used for integration, which was finer than the velocity density found using PIV and converged for the integration values.

The correlation between the average sensor response over the five experimental runs and the associated average velocity field is shown in figure 7. The scales for the velocity magnitude and the AHS current response in the figure were matched to highlight the correlation. Both the stagnation point and boundary layer separation are evident in the sensor response.

While the pie chart shows a good representation of the spatial signal response, it does not capture the variability in the AHS response. Figure 8 shows the average values and confidence intervals for the AHS response over the five runs versus the moment and force acting at the base of the hair. The error bars for the moments and forces stem from artifacts in the PIV data near the wall as shown in figure 6(b). A linear regression analysis was run for both of those data sets with

one sigma errors. The slope and intercept for the response versus the moment were 3.396×10^{1} A/(N m) and 1.193×10^{-6} A, respectively, with an r^2 of 0.679 and a standard deviation for the regression of 8.271×10^{-9} A. The slope and intercept for the response versus the force were 2.018×10^{-2} A/N and 1.194×10^{-6} A, respectively, with an r^2 of 0.658 and a standard deviation for the regression of 8.516×10^{-9} A. The similar r^2 values are a result of the velocity field near the hair tip dominating both the moment and force on the hair. Figure 9 shows the force, moment, and electrical response for the hairs as a function of heading angle.

The assembly method for this AHS prototype leads to some of the error in the sensor response, as the loose fit tolerance between the 17.6 μm OD glass fiber (hair) and the 25 μm ID pore required for the threading assembly method

4.1. Heading estimation

As a demonstration of the usefulness of the sensor, a simulation is constructed utilizing the AHS measurement data to predict the heading angle of the cylinder with respect to the incoming flow. A finite number of AHS response measurements (e.g., the current) are assumed available around the cylinder, with individual mean values (as in figure 9(b)) and standard deviations. Ideally, the sensor response is symmetric about the stagnation point, whose orientation is defined as the heading direction of the cylinder with respect to the incoming flow. To find the stagnation point, one can employ a symmetric function to fit the sampled individual senor responses based on the mean values and standard deviations, as shown in figure 10. The function chosen in the current study is a one-minus-cosine with a phase shift, given as

$$
f(\alpha) = \begin{cases} \dfrac{1}{2} A \left[1 - \cos\left(\dfrac{4\pi(\alpha - \varphi)}{R} \right) \right] & \left(\varphi - \dfrac{R}{2} \leqslant \alpha \leqslant \varphi + \dfrac{R}{2} \right) \\[4mm] 0 & \left(-180° \leqslant \alpha < \varphi - \dfrac{R}{2} \text{ or } \varphi + \dfrac{R}{2} < \alpha \leqslant 180° \right) \end{cases} \tag{4}
$$

leads to instability. Regardless, the AHS data reported in this manuscript did not show much drift over the 6 h data collection period. Note as well that these are raw sensor results containing no filtering or conditioning. The results shown here compare favorably with those from a separate test where the hairs were fabricated by growing the CNTs *in situ* with the glass fiber already in the pore. Those hairs were deployed in a highly-controlled aerodynamic experiment, where steady-state responses demonstrated excellent correlation with flow characteristics (Maschmann *et al* 2014). The data reported in this manuscript demonstrate the potential for using the piezoresistive response of the CNT coating on the hair to determine the flow features to which the hair is subjected.

where α is the heading, R and φ are the period and phase shift of the function that can be varied during the regression, and A is the constant to be determined from the regression analysis. Note that equation (4) does not include the reading of sensor currents that are not due to the impact of the incoming flow. The function is chosen as one that can closely mirror the assumed sensor readings around a cylinder, where the sensor reading (proportional to local velocity) at the stagnation point will be zero, with symmetric larger values on either side of the stagnation point leading to separation and subsequent reduction in response. The heading angle is determined by the phase shift at which the residual of the regression is minimized. When searching for the best fitted curve, the limit
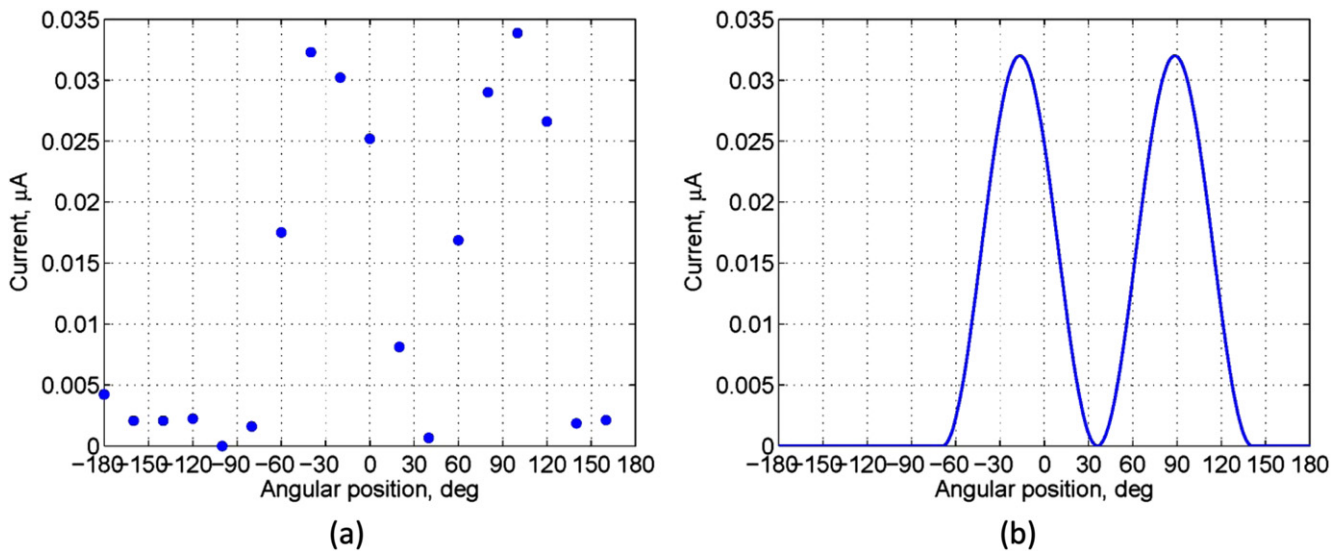

Figure 10. (a) One set of AHS response sampled from the mean values and standard deviations, (b) the function used to fit the data.
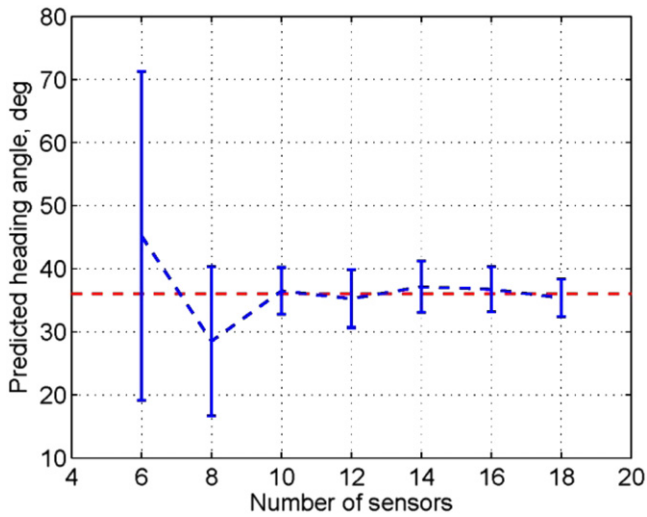
Figure 11. Comparison of heading angle predictions with different numbers of AHSs.

for the period R is from $180°$ to $220°$ and the limit for the phase φ is from $-180°$ to $+180°$.

In order to study the performance of a heading angle determination in this fashion, a series of simulations are created from the raw sensor data of figure 7. To do so, each of the sensor measurements is independently sampled 100 times to consider their distributions. The sampling randomly selects a value for each sensor based on its mean value and standard deviation. From each set of samples, a heading angle is computed. The result of this series of simulations is a set of heading predictions for a given heading angle and number of sensors, from which statistics related to the accuracy of the heading prediction can be determined.

Initially, we wish to understand the impact of the number of AHSs around the cylinder on the accuracy of the heading angle prediction. In doing so, the number of evenly distributed sensors is varied from 6 to 18. The heading predictions with variable number of sensors are compared in figure 11, where the nominal heading angle is $36°$. It is
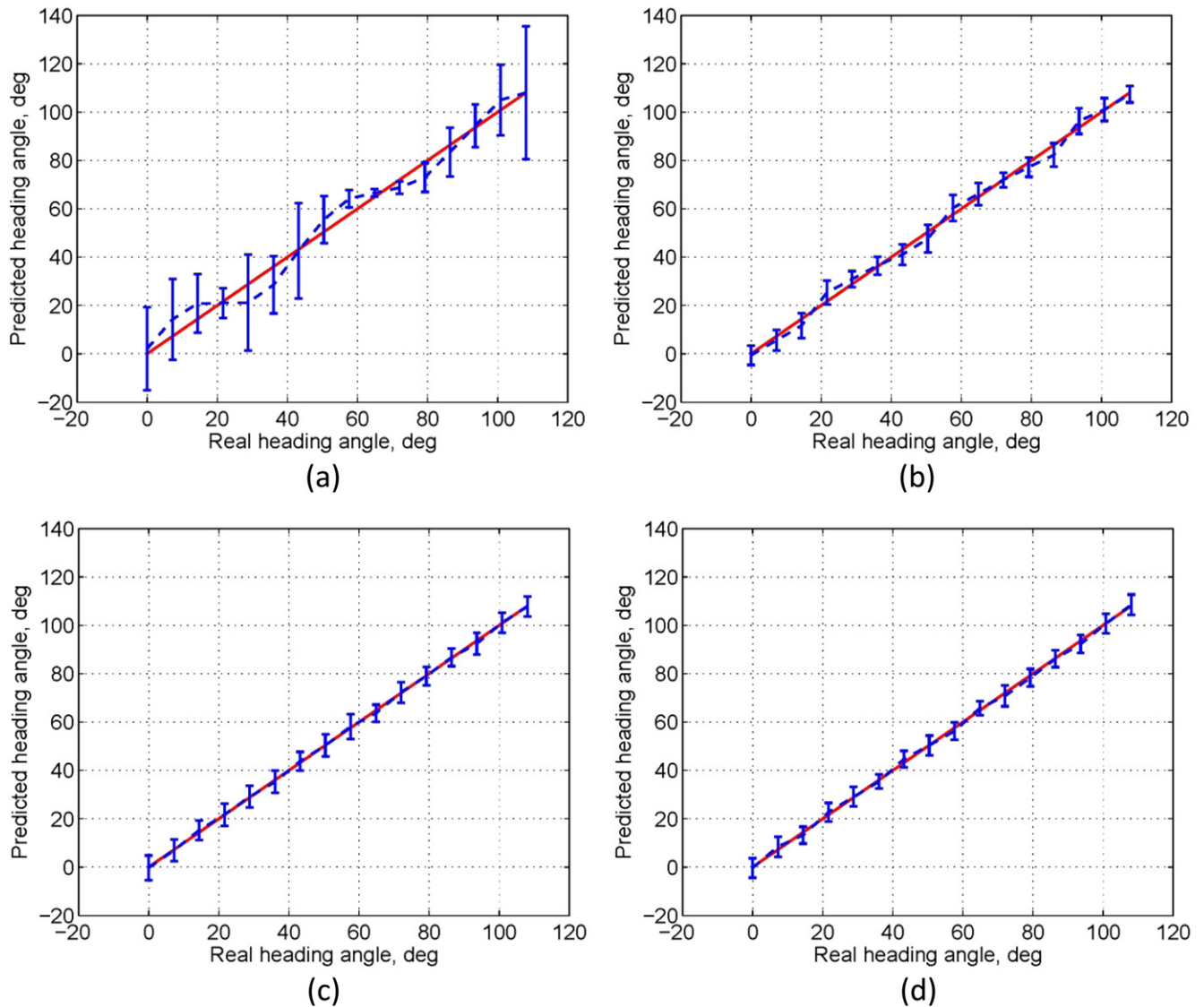

Figure 12. Predicted heading angle of the cylinder with respect to the incoming flow using different numbers of sensors: (a) 8 sensors, (b) 10 sensors, (c) 12 sensors, and (d) 18 sensors.

obvious that when there are only 6 or 8 sensors available on the circumference of the cylinder, the prediction is not accurate with a large standard deviation. When the number of sensors reaches 10 or more, the prediction is relatively consistent. Increasing the number of sensors from that point mainly helps to reduce the standard deviation of the prediction.

Figure 11 only illustrates the prediction of heading angle at one fixed orientation of the cylinder, while figure 12 shows the prediction of variable incoming flow orientations using the same approach. In the figure, the red lines represent the nominal heading angle varying from 0 to 108°, and the blue dashed lines with error bars are the predictions. The number of sensors is varied from 8, 10, 12, and 18, which correspond to the individual subplots. Overall, the prediction with 8 sensors (figure 12(a)) is erroneous. This also agrees with the observation from figure 11. For the prediction with 10 sensors (figure 12(b)), it might be acceptable at some orientations (e.g., 36° and figure 11), but the result is not stable and consistent. However, predictions with more sensors (figures 12(c) and (d)) are both accurate and consistent. From the study, it is evident that the heading angle of the cylinder can be accurately and consistently predicted even though the original AHS response measurements are noisy. In addition, the minimal number of sensors can be identified for accurate heading angle predictions. However, more sensors might be needed because of the robustness or other constraints.

Further development of the structural fiber based AHSs with a piezoresistive CNT coating has the potential to yield another useful tool for real time flow field imaging. Flight control systems can use these flow field data to autonomically make rapid adjustments to flow disturbances affecting the trajectory before the inertia and trajectory of the vehicle is significantly altered. This is becoming more critical for smaller vehicles with a low inertia that could easily be affected by flow disturbances when maneuvering in turbulent atmospheric conditions.

5. Conclusion

The response of an AHS prototype was investigated for flow features around a cylinder. This particular prototype used a 9 μm diameter, structural glass fiber as a hair and a radially aligned coating of CNTs on the hair to elicit a piezoresistive response. The flow field around the cylinder exhibited a stagnation point and a boundary layer separation but had no vortex shedding. PIV was used to map the flow field around the cylinder. The flow field data were used to calculate the force and moment acting on the base of the hair and the results were compared to the electrical response of the hair. The resulting correlation confirms the efficacy the CNT array to elicit a piezoresistive response indicative of the flow field to which the hair is subjected. While the sensor response is not exact, it fits the paradigm of 'insect grade' sensors, where redundancy is emphasized over accuracy. The simulation of heading estimation demonstrates that the sensors in their current form are sufficient for use in an aerospace application.

While this technology is still in the early stages of development, the development will augment the existing gallery of flight control sensors. The desired outcome is to develop arrays of these hair sensors to image the flow field acting on the surfaces of a vehicle for better flight control capability.

References

Bekey G 2005 *Autonomous Robots: From Biological Inspiration to Implementation and Control, Intelligent Robotics and Autonomous Agents Series* (Cambridge, MA: MIT Press)

Casas J, Steinmann T and Krijnen G 2010 Why do insects have such a high density of flow-sensing hairs? Insights from the hydromechanics of biomimetic MEMS sensors *J. R. Soc.* **7** 1487–95

Conroy J, Gremillion G, Ranganathan B and Humbert J S 2009 Implementation of wide-field integration of optic flow for autonomous quadrotor navigation *Auton. Robots* **27** 189–98

Dagamseh A M K, Wiegerink R J, Lammerink T S J and Krijnen G J M 2012 Towards a high-resolution flow camera using artificial hair sensor arrays for flow pattern observations *Bioinsp. Biomim.* **7** 046009

Devaraj H, Travas-Sejdic J, Sharma R, Aydemir N, Williams D, Haemmerle E and Aw K C 2015 Bio-inspired flow sensor from printed PEDOT: PSS micro-hairs *Bioinsp. Biomim.* **10** 016017

DeVries L, Lagor F D, Lei H, Tan X and Paley D A 2014 Distributed flow estimation and closed-loop control of an underwater vehicle with a multi-modal artificial lateral line *Bioinsp. Biomim.* **10** 025002

Dickinson B 2010 Hair receptor sensitivity to changes in laminar boundary layer shape *Bioinsp. Biomim.* **5** 016002

Dickinson B, Singler J and Batten B 2012a Mathematical modeling and simulation of biologically inspired hair receptor arrays in laminar unsteady flow separation *J. Fluids Struct.* **29** 1–17

Dickinson B T, McClain S T and Case L 2012b The dynamic response of quasi-steady hair-like structures in oscillatory boundary layer flows *6th AIAA Flow Control Conf.*

Droogendijk H, Casas J, Steinmann T and Krijnen G J M 2015 Performance assessment of bio-inspired systems: flow sensing MEMS hairs *Bioinsp. Biomim.* **10** 016001

Ehlert G J, Maschmann M R and Baur J W 2011 Electromechanical behavior of aligned carbon nanotube arrays for bio-inspired fluid flow sensors *Proc. SPIE* **7977** 79771C

Ehlert G J, Maschmann M R, Phillips D M and Baur J W 2013 Morphology control in hierarchical fibers for applications in hair flow sensors *Proc. SAMPE*

Goman M and Khrabrov A 1994 State-space representation of aerodynamic characteristics of an aircraft at high angles of attack *J. Aircr.* **31** 1109–15

Keshavan J and Humbert J 2010 MAV stability augmentation using weighted outputs from distributed hair sensor arrays *Proc. American Control Conf. (ACC)* pp 4445–50

Krijnen G, Droogendijk H, Dagamseh A, Jaganatharaja R and Casas J 2013 Imitating the cricket cercal system: the beauty of the beast with a twist of the engineer *Adv. Sci. Technol.* **84** 19–28

Mangalam A, Mangalam S and Flick P 2008 Unsteady aerodynamic observable for gust load alleviation and flutter suppression *Proc. 26th AIAA Applied Aerodynamics Conf.*

Mangalam S 2003 Phenomena-based real-time aerodynamic measurement system *Proc. IEEE Aerospace Conf.*

Maschmann M R, Dickinson B T, Ehlert G J and Baur J W 2012 Force sensitive carbon nanotube arrays for biologically inspired airflow sensing *Smart Mater. Struct.* **21** 094024

Maschmann M R, Ehlert G J, Dickinson B T, Phillips D M, Ray C W, Reich G W and Baur J W 2014 Application of individual hierarchical carbon nanotube fuzzy fibers in artificial hair plugs for air flow sensing *Adv. Mater.* **26** 3230–4

Pitcher T, Partridge B and Wardle C 1976 A blind fish can school *Science* **194** 963–5

Qualtieri A, Rizzi F, Epifani G, Ernits A, Kruusmaa M and De Vittorio M 2012 Parylene-coated bioinspired artificial hair cell for liquid flow sensing *Microelectron. Eng.* **98** 516–9

Rizzi F, Qualtieri A, Chamber L, Megill W and De Vittorio M 2013 Parylene conformal coating encapsulation as a method for advanced tuning of mechanical properties of an artificial hair cell *Soft Matter* **9** 2584–8

Rizzi F, Qualtieri A, Dattoma T, Epifani G and De Vittorio M 2015 Biomimetics of underwater hair cell sensing *Microelectron. Eng.* **132** 90–7

Sterbing-D'Angelo S, Chadha M, Chiu C, Falk B, Xian W, Barelo J and Moss C 2011 Bat wing sensors support flight control *Proc. Natl Acad. Sci.* **108** 11291–6

Tao J and Yu X 2012 Hair flow sensors: from bio-inspiration to bio-mimicking—a review *Smart Mater. Struct.* **21** 113001